

- (1995); Z. Li and L. Moreau, *J. Appl. Meteorol.* **35**, 653 (1996).
12. M.-D. Chou, A. Arking, J. Otterman, W. L. Ridgway, *Geophys. Res. Lett.* **22**, 1885 (1995).
 13. A. Arking, M.-D. Chou, W. L. Ridgway, *ibid.* **23**, 829 (1996).
 14. G. L. Stephens, *Science* **271**, 1131 (1996).
 15. C. H. Whitlock *et al.*, *Bull. Am. Meteorol. Soc.* **76**, 905 (1995).
 16. B. Barkstrom *et al.*, *ibid.* **70**, 1254 (1989). Although the ERBE all-sky average for the month is straightforward, the clear-sky average is determined by averaging only those instantaneous measurements within the grid box and within the month for which an algorithm determines that the scenes are cloud-free. Thus, it does not represent what would have been the measurement if clouds were removed, which is what the clear-sky flux represents in a model.
 17. W. B. Rossow and R. A. Schiffer, *Bull. Am. Meteorol. Soc.* **72**, 2 (1991).
 18. R. Pinker and I. Laszlo, *J. Appl. Meteorol.* **31**, 194 (1992).
 19. W. L. Darnell, W. F. Staylor, S. K. Gupta, F. M. Denn, *J. Clim.* **1**, 820 (1988).
 20. S. D. Schubert, R. B. Rood, J. Pfendner, *Bull. Am. Meteorol. Soc.* **74**, 2331 (1993).
 21. SDs for Q^T are $\sim 100 \text{ W m}^{-2}$ for both the model and the observations, but for Q^S they are $\sim 75 \text{ W m}^{-2}$ for the model and $\sim 100 \text{ W m}^{-2}$ for the GEBA observations, which indicates that the additional variability in observed Q^S might be a sampling problem.
 22. In calculating means, correlation coefficients, and regression parameters involving ratios—for example, atmospheric absorption and albedo—the data points were appropriately weighted by the incident solar flux at TOA.
 23. In multiple linear regression, the dependent variable y is represented by a variable y' , which is a linear function of several independent variables x_i . The explained variance is then the ratio of the variance of y' to the variance of y , and it represents the fraction (or percentage) of the original variance contained in y that is contained in or “explained by” y' . Hence, it is a measure of the goodness of the linear fit, and for a perfect fit the explained variance is 100%. In single linear regression there is only one independent variable, and the explained variance (as defined here) is equal to the square of the correlation coefficient.
 24. I thank Z. Li, M.-D. Chou, W. Ridgway, R. Cess, T. Charlock, and S. Warren for helpful discussions. Supported by NASA grant NAG 5-2039.

1 April 1996; accepted 18 June 1996

Subnanometer-Diameter Wires Isolated in a Polymer Matrix by Fast Polymerization

Josh H. Golden, Francis J. DiSalvo,* Jean M. J. Fréchet,*
John Silcox, Malcolm Thomas, Jim Elman

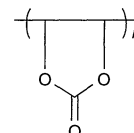
The preparation and analysis of inorganic-organic polymer nanocomposites consisting of inorganic nanowires and multiwire “cables” in a random-coil organic polymer host is reported. Dissolution of inorganic $(\text{LiMo}_3\text{Se}_3)_n$ wires in a strongly coordinating monomer, vinylene carbonate, and the use of a rapid polymerization in the presence of a cross-linking agent produce nanocomposites without phase separation. Polymerization of dilute solutions yields a material containing mostly $(\text{Mo}_3\text{Se}_3)_n$ mono- and biwires, 6 to 20 angstroms in diameter and 50 to 100 nanometers long. Polymerization of more concentrated liquid crystalline solutions yields a nanocomposite containing oriented multiwire cables, 20 to 40 angstroms in diameter and up to 1500 nanometers long, that display optical anisotropy and electrical conductivity.

The rational design and fabrication of materials that display “nanowire” or “molecular wire” morphologies is driven by potential applications in nanoscale electronic, optical, and mechanical devices (1). Useful properties exhibited by these materials include nonlinear optical phenomena, magnetism, anisotropic conductivity, and dichroism (2, 3). Some approaches used in the preparation of inorganic and organic nanofibrillar structures and composites include template synthesis of nanowires within the confines of a porous host matrix, traditional solution synthesis, and the me-

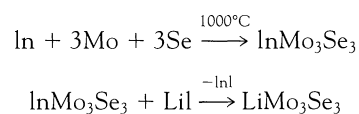
chanical dispersion of carbon and silica nanotubes within an organic polymer host (3–7).

We have prepared a nanocomposite consisting of a rigid rod metallopolymer dispersed in a random coil organic polymer host by using the “monomer as solvent” approach. This technique has been used to prepare nearly monodisperse molybdenum chloride clusters, 10 Å in diameter, isolated from one another in an organic polymer host matrix (8). The approach involves the preparation of solutions consisting of inorganic salts dissolved in an organic monomer that are bulk-polymerized in the presence of a cross-linking agent. If the monomer is chemically bound to the metal species and thus serves as a polymerizable ligand, fast solidification and chemical association of the inorganic phase with the supporting organic matrix may be achieved simultaneously. Flory has shown that rigid rods

should phase-separate in the presence of a random coil organic polymer, even at low concentrations (9). However, the use of a solvating monomer coupled to the fast polymerization of the cross-linking system about the rigid rods kinetically traps the dispersed form. The final concentration of the rigid rods in the solid nanocomposite can be tuned to yield materials that contain individual isotropic nanowires or oriented multiwire “cables.” This approach has now been extended to disperse a purely inorganic metallopolymer $(\text{LiMo}_3\text{Se}_3)_n$ (Fig. 1, A and B) in a random-coil organic polymer poly(vinylene carbonate) [poly(VC)]



We used $(\text{LiMo}_3\text{Se}_3)_n$ because it is soluble in polar solvents and has useful linear dichroism and electronic conductivity properties (10). The high solvation energy of Li^+ drives the dissolution of $(\text{LiMo}_3\text{Se}_3)_n$ to produce dark burgundy solutions (absorption maximum at 480 nm) of Li^+ cations and $(\text{Mo}_3\text{Se}_3)_n$ polyanions (10). The metallopolymer $(\text{LiMo}_3\text{Se}_3)_n$ is a member of the $(\text{MMo}_3\text{X}_3)_n$ (M, an alkali or monovalent main-group metal; X, S or Se or Te) series of metallic linear-chain compounds first described by Potel and co-workers (11) and is structurally related to the Chevrel phases (12). It is prepared (10) as shown below



The organic component, the polar monomer VC, was chosen because its chemical structure is similar to that of the nonpolymerizable solvent propylene carbonate (8), which dissolves $(\text{LiMo}_3\text{Se}_3)_n$ (10). The VC monomer retains the solubilizing property of its nonpolymerizable counterpart and polymerizes to a high molecular weight product in the presence of a free-radical generator (13). In addition, poly(VC) is an excellent supporting host for conducting Li salts (14).

A dilute inorganic-organic polymer nanocomposite containing mono- and biwires of $(\text{Mo}_3\text{Se}_3)_n$ was prepared by the thermal free-radical polymerization of 10^{-3} to 10^{-4} M VC- $(\text{LiMo}_3\text{Se}_3)_n$ solutions containing 10% by weight tris(2-hydroxyethyl) isocyanurate triacrylate (the cross-linking agent) and 2 mole percent 2,2'-azobis(2,4-dimethylvaleronitrile) (the free-radical initiator) at 23° to 50°C. The addition of a rapidly curing cross-linking agent to the

J. H. Golden, F. J. DiSalvo, J. M. J. Fréchet, Department of Chemistry, Cornell University, Baker Laboratory, Ithaca, NY 14853, USA.

J. Silcox and M. Thomas, Cornell University Materials Science Center, Clark Hall, Ithaca, NY 14853, USA.

J. Elman, Eastman Kodak Company, Rochester, NY 14650, USA.

*To whom correspondence should be addressed.

dilute solution ensured that the gel point was reached rapidly and avoided extensive aggregation of the nanowires. Complete solidification was then achieved in ~ 1 hour after the initial rapid gelling, as the remaining VC monomer polymerized to form a hard, glassy solid. The polymerization of dilute solutions may also be achieved photochemically if the thermal initiator is replaced with 5 mol% 2,2-dimethoxy-2-phenylacetophenone and a 500-W Hg lamp.

We imaged the inorganic wires in the organic polymer host (Fig. 2, A to C) by Z-contrast (Z , atomic number) scanning transmission electron microscopy (STEM) (8, 15), a technique that is sensitive to $(\text{Mo}_3\text{Se}_3)_n$ wires with high Z -number imbedded in the low Z -number poly(VC) host (intensity $\propto Z^{3/2}$). Samples for STEM analysis were prepared by polymerization of the dilute solutions on C-coated Cu grids under Ar. We estimate that the molecular weight of these $(\text{Mo}_3\text{Se}_3)_n$ wires is 1.03×10^5 , on the basis of an image length of ~ 500 Å and a $(\text{Mo}_3\text{Se}_3)_n$ unit molecular weight of 525 g mol^{-1} and an intertriangle spacing of 2.54 Å.

The presence of some defects or wire joints may be the cause of the apparent kinks in the molecular wires. However, it is more likely that these defects are the result of the two-dimensional (2D) representation of a macromolecular chain traversing a 3D volume. Because the trajectories of the individual inorganic chains cannot be re-

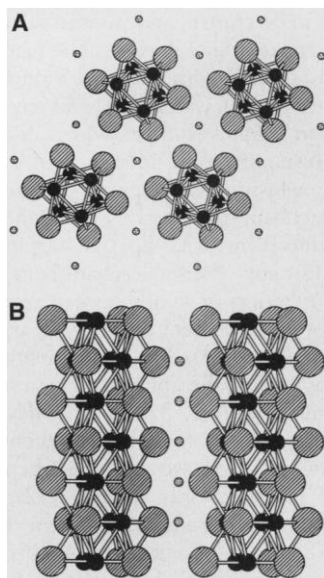


Fig. 1. (A) Projection of the $(\text{MMo}_3\text{Se}_3)_n$ structure (M , Li) onto the hexagonal (001) plane and (B) the (11 $\bar{2}$ 0) plane (side view, $n = 7$). Atoms in order of increasing size are Li, Mo, and Se. The structure is built from the polycondensation of octahedral clusters of Mo through trans triangular faces. The remaining faces are capped by the chalcogenide atoms.

stricted to a plane and the STEM depth of focus is significant (~ 400 Å), any wire bending inward from the surface would be shown as a bright spot or a kink. Wegner and co-workers have recently observed individual shape-persistent macromolecules for which 2D packing leads to a high degree of local order although defects may be clear-

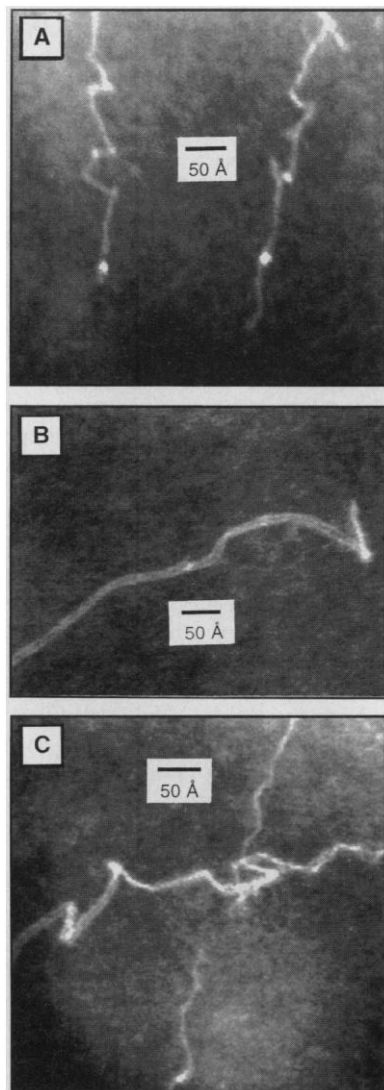


Fig. 2. Z-contrast STEM images of a 10^{-4} M nanocomposite at a magnification of 2×10^6 , 507 Å horizontal and vertical field of view (256 by 256 pixels). Because the appropriate calibration of the radiation damage and noise levels in the images has not yet been undertaken, the reader is cautioned against interpreting intensity patterns along the wires in terms of atomic structure. (A) $(\text{Mo}_3\text{Se}_3)_n$ wires 6 Å in diameter and ~ 50 nm long. The intensity variations (bright spots) are due to bends and twists in the nanowires as they traverse the host volume. (B) A biwire ~ 20 Å in diameter. Unbroken biwires can exceed 100 nm in length. (C) Intersecting mono- and biwires. As shown in the middle of the image, monowires typically suffer beam damage in 1 to 3 s, despite low current settings.

ly identified (16). However, a direct comparison of our observations (Fig. 2) with those of Wegner *et al.* is not possible because ours is not a monolayer obtained at high concentration of the polymer chains.

The flexibility of the nanowire is at first surprising because of the expected rigidity imparted by the strong intertriangle Mo–Mo bonds (bond distance = 2.54 Å, which is comparable to bond distances in Mo metal = 2.72 Å). However, the bending moment of a wire is proportional to its radius to the fourth power (17), so molecular wires will be much more flexible than macroscopic wires. Both metal whisker crystals (18) and thin films made of analogous molybdenum selenide wires (10) also exhibit considerable flexibility.

We prepared a nanocomposite containing oriented multiwire “cables” 20 to 40 Å in diameter by shearing more concentrated and viscous 0.01 M liquid crystalline VC- $(\text{LiMo}_3\text{Se}_3)_n$ solutions between two glass slides. Shearing the solution during room-temperature polymerization oriented the chains while rapid solidification (5 to 10 min under Ar) ensured retention of order. A STEM analysis of the polarizing films revealed an oriented array of multiwire cables 20 to 40 Å in diameter, containing 5 to 20 wires per cable, within the poly(VC) host (Fig. 3). A small fraction (2 to 5%) of undissolved crystallites (100 to 500 Å thick) appears to be less sensitive to the shearing forces and to orient only partially. The undissolved crystallites are a result of incomplete exchange of Li^+ for In^+ during the solid-state synthesis of $(\text{LiMo}_3\text{Se}_3)_n$, as confirmed by scanning electron microscopy microprobe analysis (19).

The oriented nanocomposite thin film (250 to 500 μm thick) exhibits significant absorption anisotropy as observed with polarized-visible absorbance microscopy and polarized-ultraviolet-visible transmission spectroscopy.

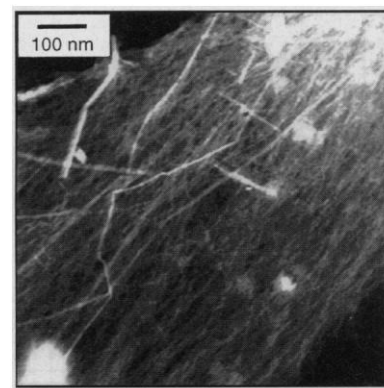


Fig. 3. A STEM dark-field image of oriented “nanocables,” 20 to 40 Å in diameter, in a 10^{-2} M polarizing film at a magnification of 3×10^5 . The field of view is 1100 nm by 1100 nm. The length of the nanocables ranges from ~ 500 to ~ 1500 nm.

copy. The transmission data yielded an average dichroic ratio (R) of 2 at 490 nm, where R is the ratio of absorbance parallel to versus perpendicular to the film (20). The conductivity of the multiwire cables in the concentrated 10^{-2} M nanocomposite was determined by an optical method because the material exhibits a high contact resistance. We estimated the conductivity from the plasma resonance (ω_p) exhibited by $(\text{LiMo}_3\text{Se}_3)_n$ in the infrared region (10). The infrared spectrum of a 10^{-2} M poly(VC)- $(\text{LiMo}_3\text{Se}_3)_n$ gel sheared between two KBr disks displays a broad $(\text{LiMo}_3\text{Se}_3)_n$ plasma absorption centered at $\sim 1100 \text{ cm}^{-1}$. Fitting the absorption according to a Drude model (21) gives ω_p and an estimated conductivity σ of 10^2 to 10^3 S cm^{-1} from $\sigma = \omega_p^2 \tau / 4\pi$, where τ is the carrier relaxation time. This compares favorably with a conductivity of $2 \times 10^2 \text{ S cm}^{-1}$ measured for a neat $(\text{LiMo}_3\text{Se}_3)_n$ thin film (10).

REFERENCES AND NOTES

1. G. M. Whitesides and J. P. Mathius, *Science* **254**, 1312 (1991); J. M. Lehn, *Angew. Chem. Int. Ed. Engl.* **29**, 1304 (1990); C. Carter, *Molecular Electronic Devices* (Dekker, New York, 1982).
2. G. Wegner *et al.*, *Mater. Res. Soc. Symp. Proc.* **328**, 15 (1994).
3. L. A. Bumm *et al.*, *Science* **271**, 1705 (1996).
4. T. M. Whitney, J. S. Jiang, P. C. Searson, C. C. Chien, *ibid.*, **261**, 1316 (1993); C. A. Huber *et al.*, *ibid.* **263**, 800 (1994).
5. R. W. Wagner and J. S. Lindsey, *J. Am. Chem. Soc.* **116**, 9759 (1994).
6. C. F. van Nostrum, S. J. Picken, R. J. M. Nolte, *Angew. Chem. Int. Ed. Engl.* **33**, 2173 (1994).
7. P. M. Ajayan, O. Stephan, C. Colliex, D. Trauth, *Science* **265**, 1212 (1994); H. Hoshino, T. Ito, N. Donkai, H. Urakawa, K. Kajiwara, *Polym. Bull.* **29**, 453 (1992).
8. J. H. Golden, H. Deng, F. J. DiSalvo, J. M. J. Fréchet, P. M. Thompson, *Science* **268**, 1463 (1995).
9. P. J. Flory, *Macromolecules* **11**, 1138 (1978).
10. J. M. Tarascon *et al.*, *J. Solid State Chem.* **58**, 290 (1985); J. H. Golden, F. J. DiSalvo, J. M. J. Fréchet, *Chem. Mater.* **7**, 232 (1995).
11. M. Potel *et al.*, *J. Solid State Chem.* **35**, 286 (1980).
12. R. Chevrel, M. Sergent, J. Prigent, *ibid.* **3**, 515 (1971).
13. Viscometric analysis of both neat poly(VC) and the poly(VC) nanocomposite yielded a chromatogram displaying a bimodal distribution and a molecular weight of $\sim 10^6$ as compared to a molecular weight of 3×10^6 for a poly(styrene) standard. Differential scanning calorimetry (DSC) from 50° to 450°C (5°C min^{-1}) revealed a broad endotherm commencing at 240°C and centered at 311°C. The polymer used for gel permeation chromatography and DSC analysis was precipitated twice from dimethyl formamide into acetone and then dried in vacuo.
14. M. L. Kaplan, E. A. Reitman, R. J. Cava, L. K. Holt, E. A. Chandross, *Solid State Ionics* **25**, 37 (1987).
15. S. J. Pennycook and L. J. Boatner, *Nature* **336**, 565 (1988). We obtained the STEM images using a Vacuum Generators HB-501A STEM at 100 keV equipped with an analytical pole piece ($C_s = 3.3 \text{ mm}$), where C_s is the spherical aberration coefficient at a working vacuum of $\sim 10^{-10}$ torr. The theoretical resolution limit is 2.7 Å.
16. J. Wu, G. Lieser, G. Wegner, *Adv. Mater.* **8**, 151 (1996).
17. L. D. Landau and E. M. Lifshitz, *Theory of Elasticity* (Pergamon, New York, 1970), p. 75.
18. C. Herring and J. K. Galt, *Phys. Rev. Ser. 2* **85**, 1060 (1952).

19. Scanning electron micrograph microprobe samples were prepared in an argon-filled inert-atmosphere box and loaded for analysis with a minimum of air exposure ($<30 \text{ s}$). We conducted the analyses using a JEOL 733 microprobe at 15 keV.
20. We acquired polarized ultraviolet-visible transmission spectra using a J. A. Woolam spectroscopic ellipsometer. Spectra were taken from 300 to 840 nm, in 7-nm increments, with the polarizer set either parallel to or perpendicular to the shearing

direction of the glass slide.

21. N. W. Ashcroft and N. D. Mermin, *Solid State Physics* (Holt, Rinehart, and Winston, New York, 1976), pp. 16–20.
22. This research was supported by the Materials Research Laboratory Program of the National Science Foundation under award DMR-9121654.

8 April 1996; accepted 29 May 1996

Visualization of Slow Axonal Transport in Vivo

Sumio Terada, Takao Nakata, Alan C. Peterson, Nobutaka Hirokawa*

In axons, cytoskeletal constituents move by slow transport. However, it remains controversial whether axonal neurofilaments are dynamic structures in which only subunits are transported or whether filaments assemble in the proximal axon and are transported intact as polymers to the axon terminus. To investigate the form neurofilament proteins take during transport, neurons of transgenic mice lacking axonal neurofilaments were infected with a recombinant adenoviral vector encoding epitope-tagged neurofilament M. Confocal and electron microscopy revealed that the virally encoded neurofilament M was transported in unpolymerized form along axonal microtubules. Thus, neurofilament proteins are probably transported as subunits or small oligomers along microtubules, which are major routes for slow axonal transport.

Neurons are highly asymmetric cells. Their axonal processes can extend for an exceptionally long distance, but there is a complete lack of protein synthesis machinery in axons. Thus, all materials necessary for axonal maintenance and function are transported from the cell body by fast and slow transport mechanisms. Components of the neuronal cytoskeleton and several axonal cytoplasmic proteins are conveyed by slow axonal transport at a rate of 0.1 to 3 mm/day (1). Although the process has been analyzed by various methods, it still remains controversial whether axonal neurofilaments are dynamic structures in which only subunits are transported (2, 3) or whether the axonal neurofilament cytoskeleton polymerizes in the cell body immediately after synthesis and subsequently is transported as a coherent column to the axon terminus by a sliding mechanism (4, 5).

To study the mechanisms involved in slow axonal transport, we constructed a recombi-

nant adenoviral vector (6) encoding an epitope-tagged neurofilament M protein. The rat gene encoding neurofilament M (7) was modified by polymerase chain reaction techniques to encode a c-Myc epitope tag (8). Because the COOH-terminus of neurofilament M is only poorly conserved among species (9), the precise amino acid sequence is unlikely to be critical, and we introduced the c-Myc epitope in that domain. The neurofilament M protein by itself cannot form 10-nm filaments (10, 11), which precludes any direct evaluation of functional consequences arising from this modification. However, in a baculovirus expression system, neurofilament M can form 10-nm filaments by copolymerizing with neurofilament L. Epitope tagging did not lead to any observable changes in cross-bridge formation, spacing between core filaments, or core filament assembly in this expression system (11). The recombinant adenovirus encoding the epitope-tagged rat neurofilament M protein (AxCA-NT-NFMmyc) was constructed by homologous recombination between the expression cosmid cassette and the parental virus genome (12). This vector was then used to infect the fourth lumbar (L4) dorsal root ganglion (DRG) neurons of both normal and transgenic mice (13). In line 44A transgenic mice, expression of an NF-H- β -galactosidase fusion protein causes the entire intermediate filament cytoskeleton to precipitate in the cell body, and consequently axons lack a neurofilament cytoskeleton (14). As neurofilament M proteins cannot by themselves form polymers (10, 11),

S. Terada, Institute for Brain Research, Faculty of Medicine, University of Tokyo, 7-3-1 Hongo, Bunkyo-ku, Tokyo 113, Japan.

T. Nakata, Department of Anatomy and Cell Biology, Faculty of Medicine, University of Tokyo, 7-3-1 Hongo, Bunkyo-ku, Tokyo 113, Japan.

A. C. Peterson, Molecular Oncology Group, McGill University, H5-35, 687 Pine Avenue West, Montreal, Quebec H3A 1A1, Canada.

N. Hirokawa, Institute for Brain Research and Department of Anatomy and Cell Biology, Faculty of Medicine, University of Tokyo, 7-3-1 Hongo, Bunkyo-ku, Tokyo 113, Japan.

*To whom correspondence should be addressed. E-mail: hirokawa@m.u-tokyo.ac.jp